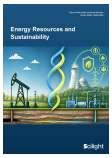
Scilight

Energy Resources and Sustainability
https://www.sciltp.com/journals/eras



Article

Numerical Simulation of Fracture Network Evolution in Supercritical CO_2 Fracturing Based on the Continuum–Discontinuum Element Method

Guopeng Huang [1], Fujian Zhou [1,*], Bo Zhang [2], Minghui Li [3], Yifan Hao [1] and Guangbo Lu [1]

[1] State Key Laboratory of Petroleum Resources and Engineering, China University of Petroleum (Beijing), Beijing 102249, China
[2] Department of Civil and Environmental Engineering, University of Alberta, Edmonton, AB T6G 1H9, Canada
[3] Oil & Gas and New Energy Branch, PetroChina Corporation, Beijing 100010, China
* Correspondence: zhoufj@cup.edu.cn

How To Cite: Huang, G.; Zhou, F.; Zhang, B.; et al. Numerical Simulation of Fracture Network Evolution in Supercritical CO_2 Fracturing Based on the Continuum–Discontinuum Element Method. *Energy Resources and Sustainability* **2026**, *1*(1), 2.

Received: 13 August 2026
Revised: 26 August 2026
Accepted: 28 August 2026
Published: 4 November 2026

Abstract: Supercritical carbon dioxide ($ScCO_2$) fracturing is a promising waterless stimulation technology for unconventional reservoirs, but the mechanisms controlling fracture-network evolution in naturally fractured formations remain unclear. In this study, a stress–flow–damage coupled numerical model based on the continuum–discontinuum element method (CDEM) was established to investigate hydraulic fracture propagation and natural fracture activation during $ScCO_2$ fracturing. Water-based fracturing and $ScCO_2$ fracturing were first compared under an identical symmetric natural fracture configuration. The effects of horizontal principal stress difference and natural fracture approach angle on fracture morphology, injection-pressure response, and fracture-width evolution were then analyzed. Finally, $ScCO_2$-induced fracture-network development in a complex natural fracture network was examined under different injection rates and stress differences. The results show that water-based fracturing is dominated by rapid pressure buildup and relatively straight main-fracture propagation, with a peak injection pressure of 22.9 MPa at 0.075 s and a fracture width of approximately 1.0 mm at 8 s. In contrast, $ScCO_2$ fracturing shows delayed pressure buildup, stronger pressure fluctuations, more pronounced natural fracture activation, and tortuous step-like fracture paths, while producing a smaller fracture width of approximately 0.44 mm at 120 s. A lower stress difference and lower approach angle favor fracture deflection and natural fracture activation, whereas a higher stress difference strengthens stress-guided main-fracture propagation. In complex fracture networks, a lower injection rate promotes more sufficient $ScCO_2$–natural fracture interaction, while a higher injection rate enhances main-fracture extension. These findings provide a numerical basis for optimizing $ScCO_2$ fracturing in naturally fractured unconventional reservoirs.

Keywords: supercritical carbon dioxide fracturing; natural fractures; fracture network; water-based hydraulic fracturing; continuum–discontinuum element method

1. Introduction

Although hydraulic fracturing has been widely applied in the development of unconventional oil and gas, geothermal energy, and uranium resources, the associated water consumption and environmental concerns have become increasingly prominent [1–3]. Supercritical carbon dioxide ($ScCO_2$) fracturing, as a representative waterless or water-reduced stimulation technique, has therefore attracted considerable attention in recent years. Under supercritical conditions, $ScCO_2$ exhibits both gas-like high diffusivity and liquid-like density, together with

Copyright: © 2026 by the authors. This is an open access article under the terms and conditions of the Creative Commons Attribution (CC BY) license (https://creativecommons.org/licenses/by/4.0/).
Publisher's Note: Scilight stays neutral with regard to jurisdictional claims in published maps and institutional affiliations.

low viscosity, low interfacial tension, and strong flow capacity in porous and fractured media [4]. Compared with water-based fracturing fluids, $ScCO_2$ can more readily penetrate rock pores, microfractures, and natural weak planes, thereby reducing fracture initiation resistance and, under favorable conditions, promoting the opening, shear slip, and reactivation of natural fractures, which facilitates the formation of complex fracture networks. In addition, $ScCO_2$ has the potential to become miscible with crude oil, reduce oil viscosity, displace adsorbed gas, and enable partial geological sequestration. These advantages make $ScCO_2$ fracturing a promising technology for the synergistic development of unconventional oil and gas resources and carbon capture, utilization, and storage (CCUS) [5,6].

However, unconventional reservoirs commonly contain discontinuities such as natural fractures, bedding planes, and weakly cemented interfaces, which can significantly alter the propagation path of induced hydraulic fractures [7–9]. When a hydraulic fracture intersects a natural fracture, various interaction modes may occur, including direct crossing, deflection, and propagation along the pre-existing fracture. The orientation, density, and length of natural fractures, as well as their angular relationship with the maximum horizontal principal stress, strongly influence the degree of connectivity between the main hydraulic fracture and the natural fracture system, thereby controlling the final fracture-network complexity and stimulated reservoir volume. Therefore, fracture propagation during $ScCO_2$ fracturing is not governed solely by fluid properties, but is jointly controlled by the fluid characteristics, *in-situ* stress state, and geometrical attributes of natural fractures [10–12].

Among the factors controlling natural fracture activation, horizontal stress difference and the approach angle of natural fractures are two key parameters governing the interaction between hydraulic fractures and natural fractures [13,14]. In general, a lower horizontal stress difference favors the deflection, opening, or shear slip of induced hydraulic fractures along pre-existing natural fractures, thereby promoting the development of complex fracture networks. In contrast, a higher horizontal stress difference strengthens the directional control of the maximum horizontal principal stress, causing the main hydraulic fracture to more readily cross natural fractures and maintain a relatively straight propagation path. Meanwhile, the natural fracture approach angle also affects the competition between fracture crossing and fracture activation. Under a low approach angle, hydraulic fractures are more likely to be captured by natural fractures and propagate along them, whereas under a high approach angle, hydraulic fractures tend to directly cross natural fractures. For $ScCO_2$ fracturing, owing to its stronger flow and penetration capacity, natural fractures may still be activated even under certain stress-difference conditions. Nevertheless, the final fracture-network morphology remains jointly constrained by the horizontal stress difference and natural fracture orientation [15].

At present, substantial understanding has been developed regarding the interaction between hydraulic fractures and natural fractures during water-based hydraulic fracturing [6,16]. However, studies on natural fracture activation, main-fracture deflection, pressure response, and fracture-width evolution under $ScCO_2$ fracturing conditions remain relatively limited. In particular, under the same natural fracture distribution, the differences between water-based fracturing and $ScCO_2$ fracturing in terms of fracture morphology, injection pressure, and fracture aperture still need to be further clarified. Moreover, the fracture-generation mechanisms of $ScCO_2$ fracturing under different natural fracture network topologies are not yet fully understood. This knowledge gap restricts the parameter optimization and engineering design of $ScCO_2$ fracturing in reservoirs with well-developed natural fractures.

Various numerical approaches have been developed to investigate fracture propagation during $ScCO_2$ fracturing. Phase-field models can represent spontaneous fracture initiation and complex crack evolution while incorporating coupled thermo-hydro-mechanical processes. Previous phase-field studies have shown that $ScCO_2$ can promote complex fracture development and that decreasing horizontal stress anisotropy facilitates fracture branching and extension [4,17], which is consistent with the present finding that a lower horizontal stress difference promotes natural-fracture activation and fracture-network complexity. Displacement-discontinuity and boundary-element-based approaches are computationally efficient for explicitly representing propagating fracture surfaces. Zhao et al. [11], for example, reported that CO_2 fracturing in naturally fractured reservoirs produces relatively narrower fractures and activates more natural fractures than conventional water-based fracturing, which agrees with the major trends obtained in the present simulations. Numerical models incorporating discrete fracture networks have further demonstrated that fracture evolution is strongly controlled by the geometry and spatial distribution of pre-existing discontinuities, as well as by the *in-situ* stress state and injection conditions [18]. Despite these advances, different numerical approaches have distinct capabilities and limitations. Phase-field methods are well suited for spontaneous crack evolution and thermo-hydro-mechanical coupling but generally require regularization parameters and relatively fine spatial discretization, whereas displacement-discontinuity, boundary-element, and discrete fracture network (DFN)-based approaches are particularly effective for explicitly represented fracture systems. In comparison, CDEM combines continuum deformation of the rock matrix with

explicit discontinuous interface failure within a unified framework, allowing tensile opening, shear slip, fracture deflection, crossing, coalescence, and natural-fracture activation to be represented during hydraulic-fracture–natural-fracture interaction [19–21]. Therefore, CDEM provides a suitable framework for investigating the complex fracture-network evolution induced by $ScCO_2$ in naturally fractured reservoirs.

Based on this background, a stress–seepage–damage coupled numerical model based on the continuum–discontinuum element method was established to investigate the propagation behavior of $ScCO_2$-induced fracture networks in naturally fractured reservoirs. First, under the same symmetric natural fracture distribution, the differences between water-based fracturing and $ScCO_2$ fracturing were comparatively analyzed in terms of fracture propagation morphology, injection-pressure evolution, and fracture-width variation. Second, the effects of horizontal stress difference and natural fracture approach angle on the main-fracture propagation path, natural fracture activation, and fracture complexity were systematically examined. Finally, the fracture-generation behavior of $ScCO_2$ fracturing under different natural fracture network conditions was further discussed. This study provides a theoretical basis for the design of $ScCO_2$ fracturing in unconventional reservoirs with well-developed natural fractures, and also offers a numerical reference for injectivity evaluation and fracture-network evolution prediction during CO_2 geological sequestration.

2. Methodology

2.1. Solid Mechanical Formulation

The hydraulic fracturing and $ScCO_2$ fracturing processes were simulated using the continuum–discontinuum element method (CDEM). In this framework, the rock matrix is discretized into block elements to describe continuum deformation, while the interfaces between adjacent blocks represent potential discontinuities, including hydraulic fractures, natural fractures and weak planes. The CDEM framework combines finite-element-based deformation calculation with discrete interface failure, allowing the model to capture the transition from continuous deformation to fracture initiation, propagation and interaction with pre-existing discontinuities.

Following the CDEM formulation used for hydraulic–natural fracture interaction, the dynamic equilibrium of an element can be written as [21]:

$$\mathbf{M}\ddot{\mathbf{u}}^{\boldsymbol{e}} + \mathbf{C}\dot{\mathbf{u}}^{\boldsymbol{e}} + \mathbf{K}\mathbf{u}^{\boldsymbol{e}} = \mathbf{F}^{\boldsymbol{e}} \tag{1}$$

where $\mathbf{M}$, $\mathbf{C}$ and $\mathbf{K}$ are the element mass, damping and stiffness matrices, respectively; $\mathbf{u}^{\boldsymbol{e}}$, $\dot{\mathbf{u}}^{\boldsymbol{e}}$ and $\ddot{\mathbf{u}}^{\boldsymbol{e}}$ denote the nodal displacement, velocity and acceleration vectors of element $\boldsymbol{e}$; and $\mathbf{F}^{\boldsymbol{e}}$ is the external nodal force vector.

The transient mechanical response is advanced by the explicit Euler forward-difference scheme adopted in CDEM:

$$\dot{\mathbf{u}}^{n+1} = \dot{\mathbf{u}}^{n} + \ddot{\mathbf{u}}^{n}\Delta\boldsymbol{t}, \qquad \mathbf{u}^{n+1} = \mathbf{u}^{n} + \dot{\mathbf{u}}^{n+1}\Delta\boldsymbol{t} \tag{2}$$

where n is the time-step index and $\Delta\boldsymbol{t}$ is the time increment.

2.2. Interface Deformation and Fracture Criteria

The transition from continuous deformation to discontinuous fracturing is controlled by interface springs between adjacent blocks. Before failure, the normal and tangential spring deformations follow Hooke-type relations in the CDEM [19].

$$\Delta u_n = \frac{F_n}{K_n} = \frac{(\sigma_{n1} + \sigma_{n2})A}{2K_n} \tag{3}$$

where Δu_n is the normal relative displacement of the interface spring, F_n is the normal contact force, K_n is the normal spring stiffness, σ_{n1} and σ_{n2} are the normal stresses at the two adjacent contact sides, and A is the contact area.

$$\Delta u_t = \frac{F_t}{K_t} = \frac{(\sigma_{t1} + \sigma_{t2})A}{2K_t} \tag{4}$$

where Δu_t is the tangential relative displacement of the interface spring, F_t is the tangential contact force, K_t is the tangential spring stiffness, σ_{t1} and σ_{t2} are the tangential stresses at the two adjacent contact sides, and A is the contact area.

Interface failure is evaluated by the maximum tensile stress criterion and the Mohr-Coulomb shear criterion, which are commonly used in CDEM fracture simulations to distinguish tensile failure from shear failure:

$$\sigma_n \geq T \tag{5}$$

where σ_n is the normal stress and T is the tensile strength of the rock material.

$$\sigma_t > c + \sigma_n \tan\varphi \tag{6}$$

where σ_t is the tangential stress, c is the cohesion, σ_n is the normal stress, and φ is the internal friction angle. When Equation (5) is satisfied, the interface is classified as tensile failure; when Equation (6) is satisfied, it is classified as shear failure.

2.3. Fluid Flow and Hydro-Mechanical Coupling

Fluid transport in the fracture network is represented by the cubic law for flow between fracture surfaces, as used in CDEM-based hydraulic-fracturing simulations [20].

$$v_f = -\frac{w_f^2}{12\mu}\nabla p_f \tag{7}$$

where v_f is the aperture-averaged fluid velocity in the fracture, w_f is the local fracture aperture, μ is the dynamic viscosity of the fracturing fluid, and p_f is the fracture-fluid pressure.

For pore flow in the matrix, the same CDEM fluid-flow formulation adopts Darcy's law:

$$v_i = -\frac{k_i}{\mu} k_s \frac{\partial p_e}{\partial x_i} \tag{8}$$

where v_i is the pore-fluid velocity component in the *i* direction, k_i is the absolute permeability component in the i direction, μ is the dynamic viscosity, k_s is the relative permeability, p_e is the pore pressure in the matrix element, and x_i is the spatial coordinate in the *i* direction.

The exchange flow between porous matrix elements and fracture elements is also calculated using Darcy's law in the CDEM fluid-solid coupling scheme [22]:

$$Q_{ef} = -\frac{k_e}{\mu}\frac{p_e - p_f}{d} A \tag{9}$$

where Q_{ef} is the matrix-fracture exchange flow rate, k_e is the matrix permeability, p_e is the average pore pressure in the matrix element, p_f is the average fluid pressure in the fracture element, d is the distance from the matrix centroid to the fracture plane, and A is the effective matrix-fracture exchange area.

The fluid pressure obtained from the fracture and matrix flow calculations is applied to the mechanical interfaces, changing the normal effective stress and the spring response. Conversely, fracture opening and slip modify the aperture and therefore the hydraulic conductance in Equation (7). This two-way coupling enables the model to capture direct fracture crossing, arrest, offset propagation, tensile opening of natural fractures and shear activation along weak natural discontinuities.

The CDEM-based stress–seepage–damage coupling framework adopted in this study has been previously benchmarked under conventional water-based hydraulic-fracturing conditions. Comparisons with the classical Khristianovich–Geertsma–de Klerk (KGD) analytical solution showed good agreement in fracture-length and fracture-width evolution, while hydraulic-fracture–natural-fracture interaction modes were also validated against published analytical and experimental results [9,19]. These previous validations provide the basis for the mechanical, fracture-failure, and hydro-mechanical coupling formulations employed in the present study.

3. Model Description

To investigate fracture propagation and natural fracture activation during water-based and supercritical CO_2 ($ScCO_2$) fracturing, a two-dimensional numerical model with a size of 8 m × 8 m was established. A fluid injection point was placed at the center of the model, where the fracturing fluid was injected at a constant injection rate. Two pre-existing natural fractures, each with a length of 2 m, were symmetrically arranged on both sides of the injection point. The model was discretized using unstructured triangular meshes with a mesh size of 0.1 m. Displacement constraints were applied to the external solid boundaries, and the initial *in-situ* stress field was then initialized. The horizontal stress difference was defined as $\Delta\sigma = \sigma_H - \sigma_h$, where σ_H and σ_h denote the maximum and minimum horizontal principal stresses, respectively. To evaluate the effect of stress anisotropy on fracture propagation, three stress-difference cases of $\Delta\sigma = 2$ MPa, 5 MPa, and 10 MPa were designed by varying σ_H while keeping σ_h constant. To examine the influence of natural fracture orientation on fracture propagation, the angle between the maximum horizontal principal stress direction and the natural fracture was defined as the natural fracture approach angle, which was set to 30°, 60°, and 90°, respectively. Figure 1 shows the physical model and mesh configuration for the case with an approach angle of 60°. The model contains 16,820 block elements and

25,390 interface elements. All water-based and $ScCO_2$ fracturing cases used the same geometric model, mesh size, boundary conditions, and injection scheme. $ScCO_2$ was represented using an equivalent single-phase fluid formulation. Its density variation was incorporated through fluid compressibility, whereas its viscosity was treated as a constant. The main properties of the rock, water-based fracturing fluid, and supercritical CO_2 are listed in Table 1. The mechanical properties of the rock matrix and natural fractures were chosen within representative ranges reported for unconventional reservoir rocks and mechanically weak pre-existing discontinuities [9,12,19].

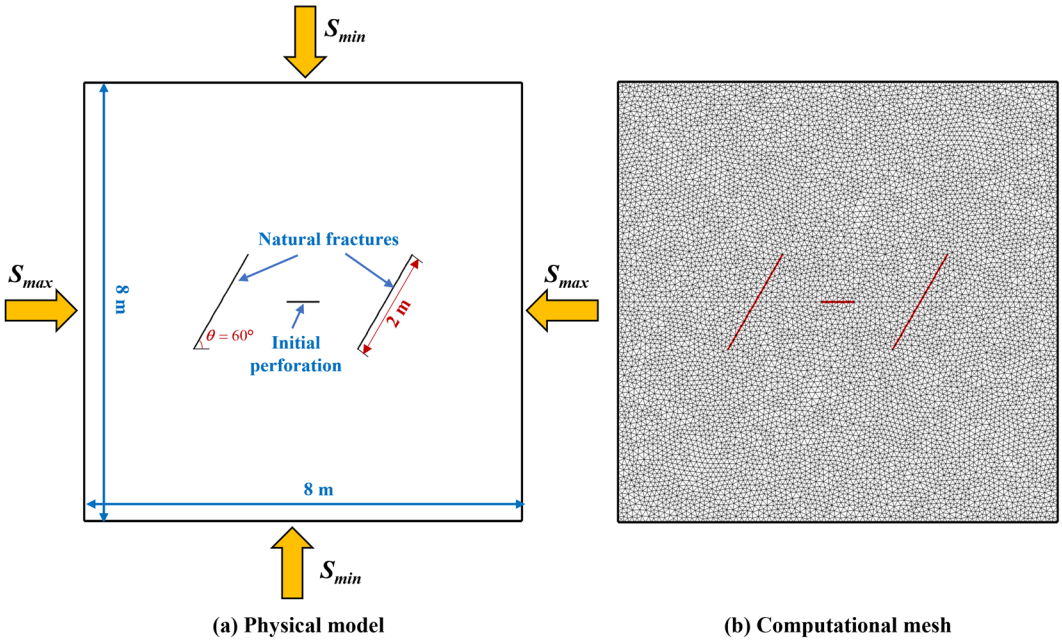


Figure 1. Schematic diagram of the physical model and the mesh discretization.

Table 1. Main mechanical parameters and fluid properties in the numerical model.

Type	Parameter	Value	Parameter	Value
Rock matrix	Young's modulus/GPa	35	Poisson's ratio	0.25
	Tensile strength/MPa	8	Cohesion/MPa	15
Natural fracture	Tensile strength/MPa	2	Cohesion/MPa	4
	Internal friction angle/°	20		
In-situ stress	Minimum effective principal stress/MPa	5	Maximum effective principal stress/MPa	10
Water	Density/(kg/m^3)	1000	Viscosity/(mPa·s)	1
$ScCO_2$	Reference density/(kg/m^3)	700	Viscosity/(mPa·s)	0.05
Injection condition	Injection rate/(m^3/s)	0.001		

4. Results and Analysis

4.1. Comparison between Water-Based Fracturing and $ScCO_2$ Fracturing

Figure 2 compares the fracture propagation patterns induced by water-based fracturing and $ScCO_2$ fracturing under the horizontal stress difference of 5 MPa and the natural fracture approach angle of 60°. Both fracturing fluids initiated a main hydraulic fracture near the injection point and promoted its propagation along the direction of the maximum horizontal principal stress. However, clear differences can be observed in fracture aperture distribution and natural fracture activation. Under water-based fracturing, the main fracture primarily propagated along the maximum horizontal principal stress direction, and only local natural fracture activation occurred after the hydraulic fracture intersected the pre-existing natural fractures. In contrast, under $ScCO_2$ fracturing, the fracture was more prone to deflection when approaching the natural fractures and subsequently propagated along the natural fracture direction. Pronounced fracture deflection and step-like propagation were observed near the natural fractures on both sides, indicating that low-viscosity CO_2 more readily invades pre-existing natural fractures, modifies the local stress state, and induces natural fracture opening or shear slip. Nevertheless, the fracture aperture generated by $ScCO_2$ fracturing was generally smaller than that generated by water-based fracturing. Overall, the properties of the fracturing fluid play a significant role in controlling fracture propagation in naturally fractured

reservoirs: water-based fracturing is characterized by main-fracture-dominated propagation, whereas $ScCO_2$ fracturing exhibits a stronger tendency for natural fracture activation and tortuous fracture-path development.

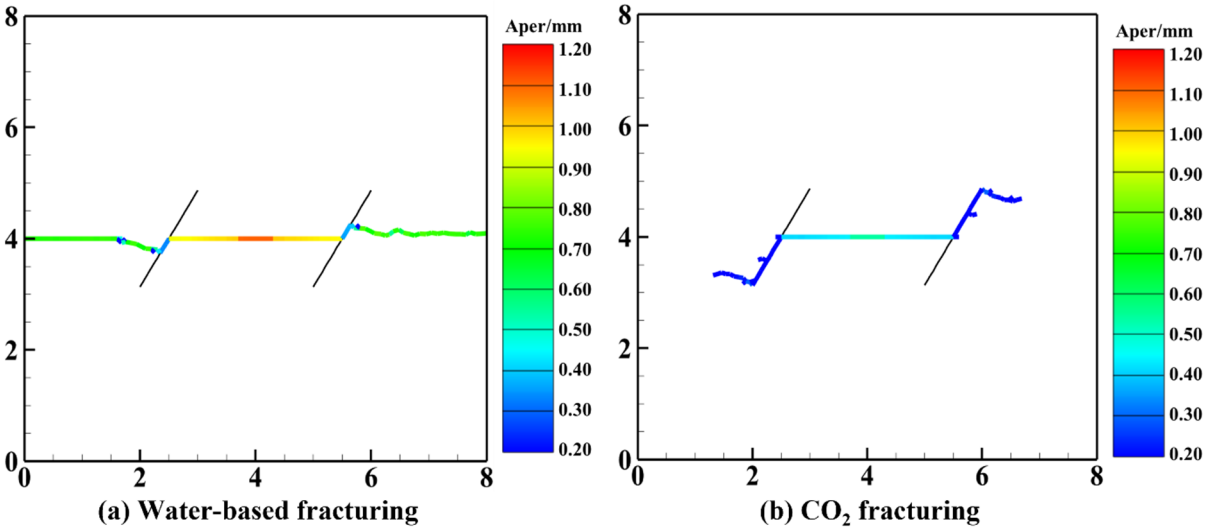


Figure 2. The fracture propagation patterns induced by water-based fracturing and $ScCO_2$ fracturing.

To quantitatively characterize the difference in fracture-path geometry, fracture tortuosity was calculated as

$$T = \frac{L_p}{L_s} \tag{10}$$

where L_p is the actual fracture-path length from the injection point to the fracture tip and L_s is the corresponding straight-line distance. The average tortuosity of the two principal fracture wings was 1.058 for water-based fracturing and 1.164 for $ScCO_2$ fracturing, corresponding to an increase of approximately 10%. This quantitative result confirms that $ScCO_2$ induces a more tortuous propagation path.

Figure 3 compares the injection-pressure and fracture width evolution during water-based fracturing and $ScCO_2$ fracturing. For water-based fracturing, the injection pressure increased rapidly at the early stage and reached a peak value of 22.9 MPa at 0.075 s. Subsequently, a pronounced pressure drop occurred due to fracture initiation and rapid fracture propagation, followed by a gradual pressure recovery and slow increase. In contrast, the pressure buildup during $ScCO_2$ fracturing was significantly delayed. The injection pressure increased slowly over a relatively long period and reached a peak value of 22.3 MPa at approximately 7.33 s, followed by a rapid pressure drop and a fluctuating propagation stage. This indicates that the low compressibility of the water-based fracturing fluid enables rapid pressure buildup at the injection point and within the fracture, thereby promoting rapid main-fracture initiation. By contrast, owing to the high compressibility of CO_2, part of the injected energy is first consumed by fluid compression and pressure accumulation, resulting in a delayed pressure response. The pronounced pressure fluctuations after the peak pressure during $ScCO_2$ fracturing are mainly associated with natural fracture opening, fracture deflection, and local pressure release, indicating stronger interactions between CO_2 and the natural fractures. The fracture width evolution further demonstrates the distinct effects of the two fracturing fluids on fracture aperture. Under water-based fracturing, the fracture width increased rapidly after fracture initiation, and the fracture width at the injection point reached approximately 1.0 mm at 8 s. In contrast, the fracture-width growth during $ScCO_2$ fracturing was markedly delayed, and the fracture width at the injection point was approximately 0.44 mm at 120 s, which was significantly smaller than that in the water-based fracturing case. This behavior is mainly attributed to the low viscosity and high compressibility of CO_2. The low viscosity facilitates CO_2 invasion into natural fractures and promotes a more complex fracture path, but it also enhances fluid diversion and pressure dissipation. Meanwhile, the high compressibility weakens the rapid accumulation of net pressure within the fracture, thereby limiting fracture-width growth.

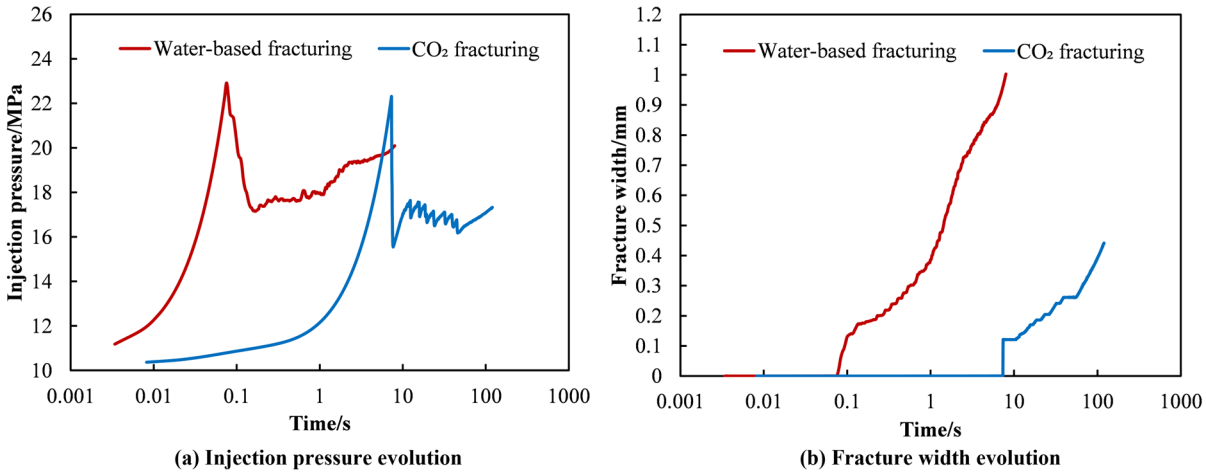


Figure 3. The injection-pressure and fracture width evolution during water-based fracturing and $ScCO_2$ fracturing.

4.2. The Effect of Stress Difference

Figure 4 compares the fracture propagation patterns induced by water-based fracturing and $ScCO_2$ fracturing under different horizontal stress differences. The results show that the horizontal stress difference has a significant influence on fracture propagation paths and natural fracture activation, while the responses of the two fracturing fluids to stress difference are markedly different. For water-based fracturing, when the stress difference is 2 MPa, the main fracture exhibits pronounced deflection during propagation. After intersecting the natural fractures, the natural fractures are activated and the fracture propagates along their directions. As the stress difference increases to 5 MPa, the main fracture tends to propagate along the direction of the maximum horizontal principal stress, with only slight disturbance near the natural fractures, indicating a weakened degree of natural fracture activation. When the stress difference further increases to 10 MPa, the fracture mainly propagates along the maximum horizontal principal stress direction and directly crosses the natural fractures on both sides. These results indicate that, for water-based fracturing, an increase in horizontal stress difference strengthens the control of the principal stress direction on fracture propagation, suppresses fracture deflection and natural fracture activation, and promotes a transition from a deflected propagation mode to a planar main-fracture-dominated mode. Compared with water-based fracturing, $ScCO_2$ fracturing shows more pronounced natural fracture activation and tortuous fracture propagation under different stress-difference conditions. At a stress difference of 2 MPa, the CO_2-driven fractures are clearly deflected near the natural fractures on both sides and propagate along the natural fracture directions. When the stress difference increases to 5 MPa, the horizontal extension of the main fracture becomes more evident, whereas the natural fractures are still significantly activated, indicating that low-viscosity CO_2 maintains a strong ability to invade pre-existing weak planes. As the stress difference further increases to 10 MPa, the main fracture continues to propagate along the maximum horizontal principal stress direction under stronger stress guidance. After intersecting the natural fractures on both sides, it induces natural fracture opening, and the fracture further propagates toward both ends of the natural fractures. Therefore, under the symmetric natural fracture configuration considered in this study, a high stress difference does not completely suppress the activation of natural fractures by CO_2. Instead, the stronger stress guidance enables the main fracture to connect the natural fractures more stably on both sides, thereby inducing their opening and local extension.

Figure 5a shows the effect of horizontal stress difference on the injection pressure evolution during water-based fracturing. The results indicate that the injection pressure increases rapidly at the initial stage and reaches a short-lived peak, followed by a rapid decrease to approximately 17–18 MPa due to fracture initiation and rapid fracture propagation. During the subsequent fracture-extension stage, all three pressure curves show a gradual increasing trend, but their growth rates differ. The pressure in the 10 MPa case increases most rapidly and is higher than that in the 5 MPa and 2 MPa cases within a shorter time, indicating that a higher horizontal stress difference strengthens the stress constraint on fracture opening and extension, thereby requiring a higher net pressure for continued fracture propagation. Figure 5b shows the effect of horizontal stress difference on the injection-pressure evolution during $ScCO_2$ fracturing. The injection pressure also increases rapidly at the initial stage, followed by a pronounced pressure drop to approximately 16–18 MPa. Subsequently, the pressure curves exhibit multiple fluctuations and step-like decreases/recoveries, indicating that fracture propagation is accompanied by staged pressure release associated with local failure, fracture connection, natural fracture opening, or shear slip. In addition, the pressure fluctuations are more pronounced under lower stress-difference conditions, suggesting that

fracture paths are more easily controlled and dynamically adjusted by natural fractures when stress anisotropy is weak, resulting in a more complex and unstable fracture-network evolution process.

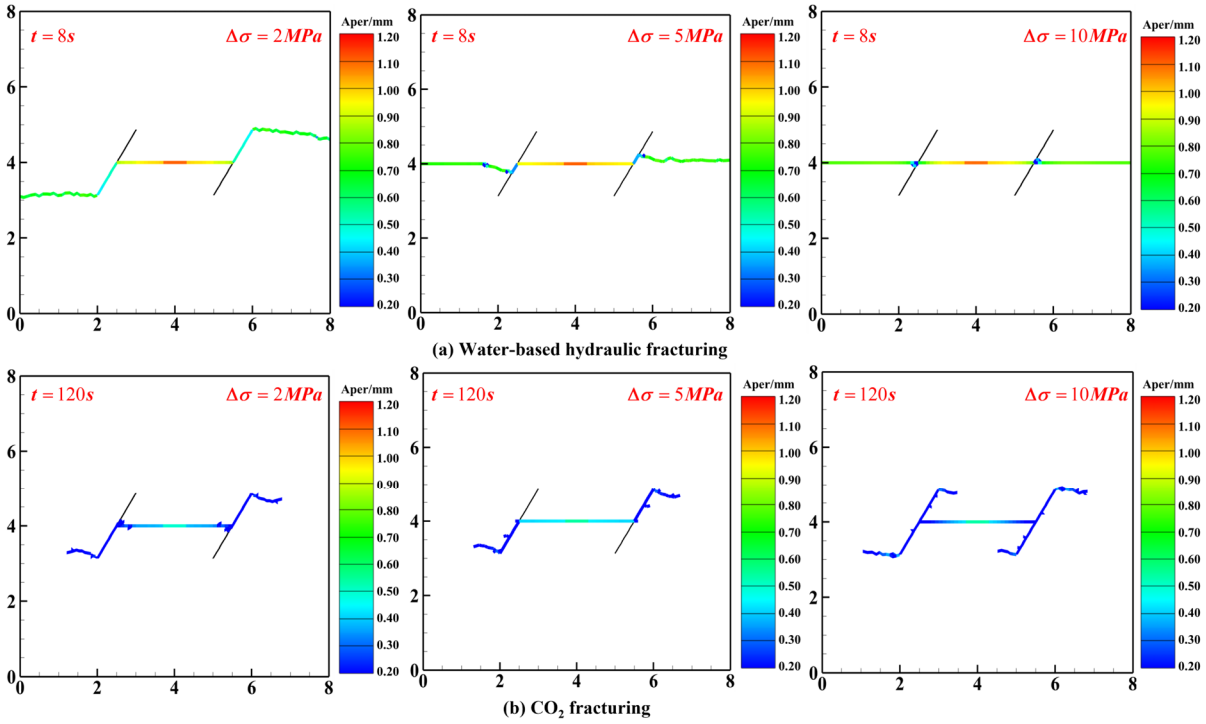


Figure 4. The fracture propagation patterns induced by water-based fracturing and $ScCO_2$ fracturing under different horizontal stress differences.

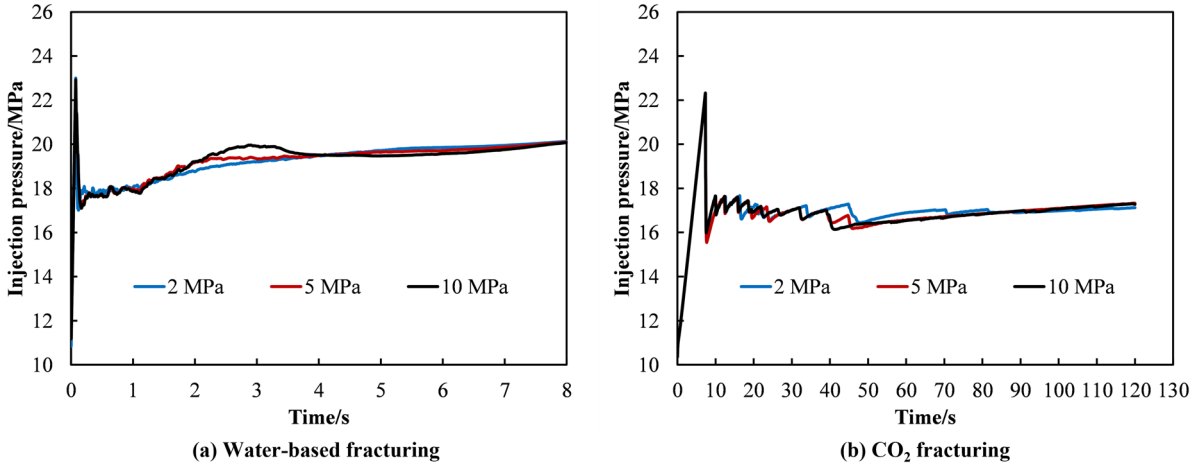


Figure 5. The injection pressure evolution during water-based fracturing and $ScCO_2$ fracturing under different horizontal stress differences.

Figure 6 shows the fracture width evolution during water-based fracturing and $ScCO_2$ fracturing under different horizontal stress differences. Overall, the fracture width increases progressively with injection time under both fluid conditions, although the growth characteristics are markedly different. Figure 6a presents the results for water-based fracturing. The fracture width increases rapidly at the initial stage, followed by a gradual reduction in the growth rate, and then continues to increase slowly at the later stage. With increasing stress difference, the fracture width generally becomes larger during the early and intermediate stages. It should be noted that the three curves exhibit a synchronous upward trend again at the later stage, which is mainly associated with fracture propagation approaching the model boundaries. Figure 6b presents the results for $ScCO_2$ fracturing. Compared with water-based fracturing, the fracture width under $ScCO_2$ fracturing increases much more slowly, and the final fracture width is approximately 0.40–0.45 mm, which is significantly smaller than that in the water-based fracturing cases. The fracture-width curves exhibit a step-like growth pattern, which may be associated with local fracture propagation, natural fracture activation, and pressure redistribution. Under different stress difference

conditions, the 5 MPa and 10 MPa cases show relatively larger fracture widths at the later stage, whereas the final fracture width in the 2 MPa case is comparatively smaller. This suggests that, under a lower stress difference, the fluid is more likely to be diverted into natural fractures, which weakens the net-pressure buildup within the main fracture and consequently limits further fracture opening.

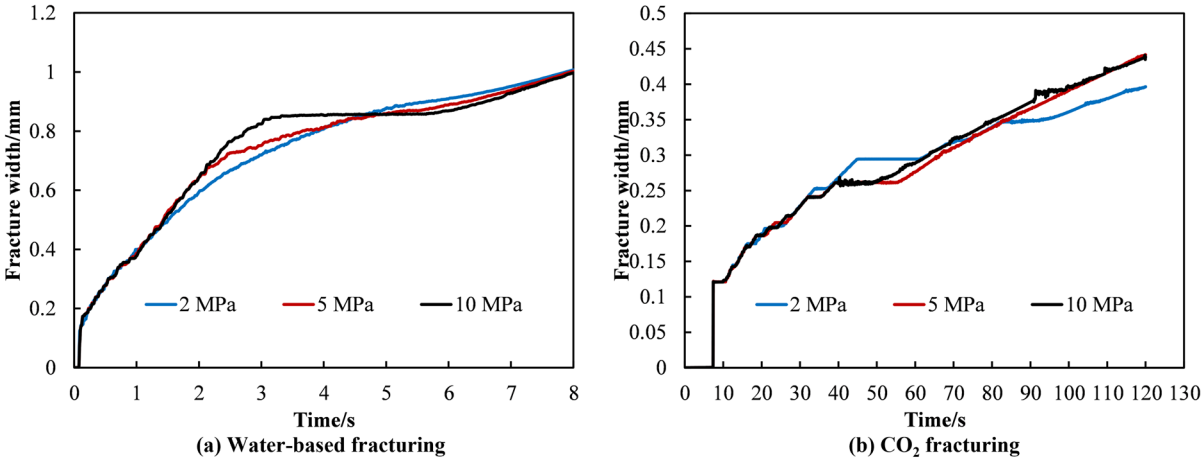


Figure 6. The fracture width evolution during water-based fracturing and $ScCO_2$ fracturing under different horizontal stress differences.

4.3. The Effect of Natural Fracture Approach Angle

Figure 7 compares the fracture propagation patterns induced by water-based fracturing and $ScCO_2$ fracturing under different natural fracture approach angles. The results show that the main fractures propagate horizontally under all natural fracture angle conditions and interact with the natural fractures on both sides to varying degrees. When $\theta = 30°$, the main fracture exhibits pronounced deflection after approaching the natural fractures and subsequently propagates along the natural fracture direction, indicating that low-angle natural fractures are more likely to induce fracture turning and participate in fracture-network formation. When $\theta = 60°$, local deflection occurs after the main fracture intersects the natural fractures, while the overall propagation path still maintains a clear horizontal trend. This suggests that natural fractures at this angle disturb the main-fracture path to some extent, but their controlling effect is weaker than that in the 30° case. When $\theta = 90°$, the main fracture generally maintains horizontal propagation, and no natural fracture activation or deflected propagation is observed. For $ScCO_2$ fracturing, when $\theta = 30°$, the main fracture activates the natural fractures after connecting with them and further propagates along the natural fracture direction. When $\theta = 60°$, the hydraulic fracture also activates the natural fractures, accompanied by the formation of local branch fractures. In contrast, when $\theta = 90°$, the main fracture still mainly propagates horizontally across the model, and the two vertical natural fractures have a limited influence on the fracture propagation path, resulting in the simplest fracture geometry.

Figure 8 shows the evolution of injection pressure with time under different natural fracture approach angles. Overall, both water-based fracturing and $ScCO_2$ fracturing exhibit a pressure response characterized by rapid pressure buildup, a sharp post-peak pressure drop, and subsequent gradual adjustment. However, the effect of natural fracture approach angles differs between the two fracturing fluids. Figure 8a presents the results for water-based fracturing. The injection-pressure curves show only minor differences under different natural fracture approach angles. Nevertheless, the injection pressure in the 60° case is slightly higher than that in the 30° and 90° cases during the intermediate stage, indicating that relatively higher injection pressure is required to sustain fracture propagation at this angle. This may be related to the competing effects of fracture crossing, deflection, and local natural fracture activation. Figure 8b presents the results for $ScCO_2$ fracturing. Compared with water-based fracturing, $ScCO_2$ fracturing exhibits more pronounced periodic fluctuations and step-like pressure adjustments, indicating more frequent natural fracture activation, local fracture connection, and pressure release during fracture propagation. Among the different angle cases, the 30° case shows the most significant pressure fluctuations during the early and intermediate stages and exhibits an earlier pressure drop, suggesting that low-angle natural fractures are more likely to connect with the main fracture and induce fracture deflection. The 60° case shows a moderate degree of pressure fluctuation, whereas the 90° case exhibits relatively weak pressure fluctuations, indicating that high-angle natural fractures have a limited disturbance effect on the main fracture propagation path and that the fracture propagation process is relatively stable.

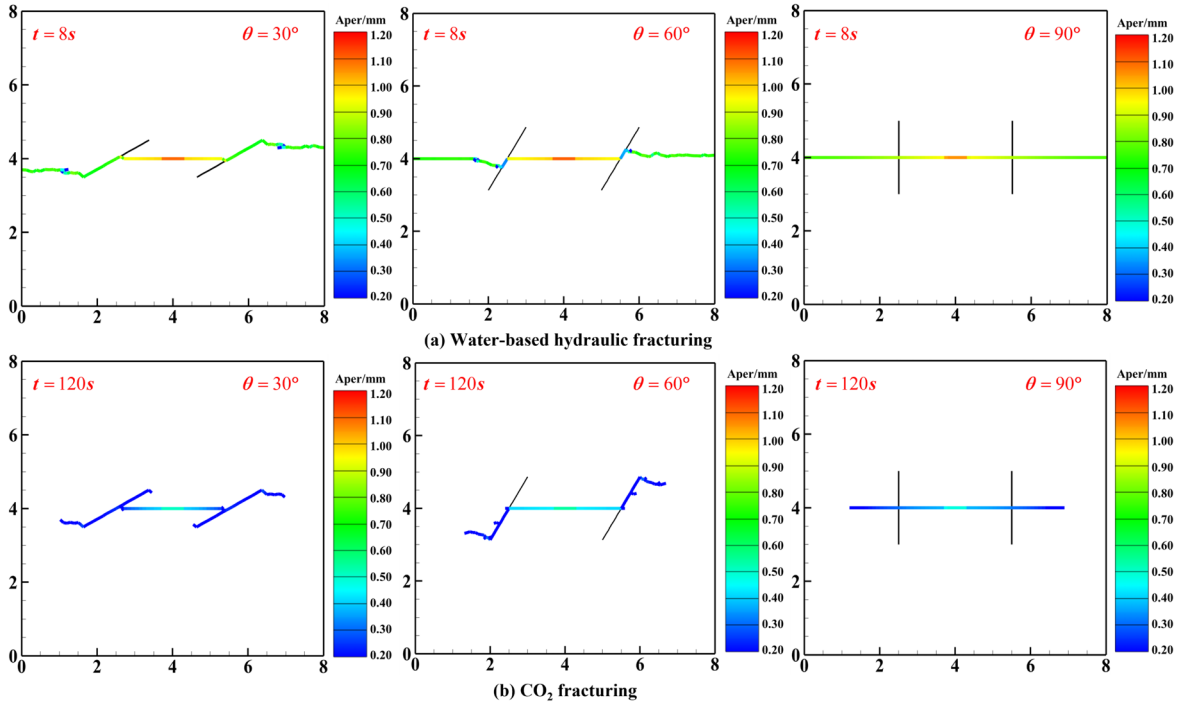


Figure 7. The fracture propagation patterns induced by water-based fracturing and $ScCO_2$ fracturing under different natural fracture approach angles.

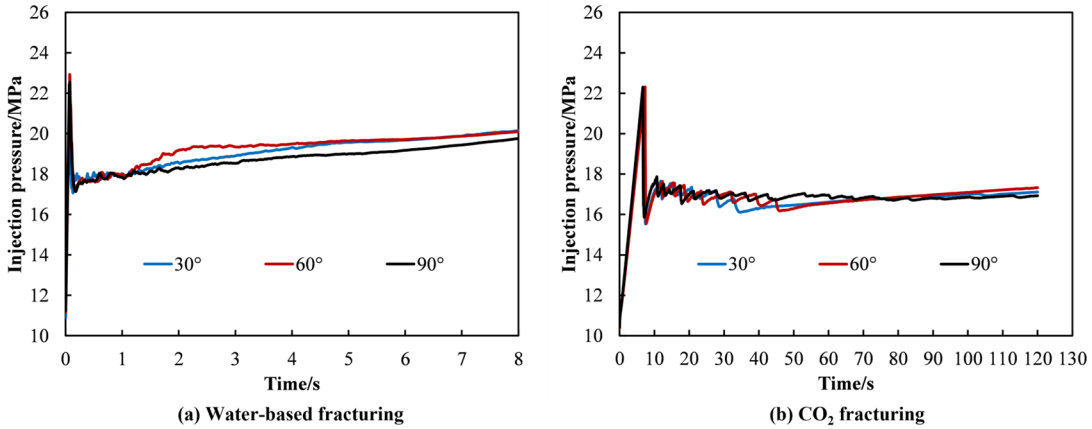


Figure 8. The injection pressure evolution during water-based fracturing and $ScCO_2$ fracturing under different natural fracture approach angles.

Figure 9 shows the evolution of fracture width with time under different natural fracture approach angles. Overall, the fracture width increases gradually with injection time under both water-based fracturing and $ScCO_2$ fracturing, but the growth magnitude and stage characteristics differ significantly between the two fluids. Figure 9a presents the results for water-based fracturing. The fracture width increases rapidly at the initial stage, followed by a gradual decrease in the growth rate. Among the different angle cases, the 60° case exhibits the largest fracture width, followed by the 30° case, while the 90° case shows a relatively smaller fracture width. Figure 9b presents the results for $ScCO_2$ fracturing. Compared with water-based fracturing, the fracture width under $ScCO_2$ fracturing is generally smaller, with a final width of approximately 0.38–0.44 mm, which is significantly lower than that in the water-based fracturing cases. The curves show a certain step-like growth pattern, indicating that fracture-aperture growth is accompanied by local fracture propagation, natural fracture activation, or pressure redistribution. Among the different angle cases, the 60° case shows the largest fracture width at the later stage, followed by the 30° case, while the 90° case exhibits the smallest fracture width. Overall, water-based fracturing can generate larger fracture widths, whereas $ScCO_2$ fracturing produces smaller fracture widths because its low viscosity and strong leak-off capacity make it more difficult to maintain net pressure within the fracture. The natural fracture angle has a significant influence on fracture aperture, and the 60° case shows relatively larger fracture widths under both fluid conditions.

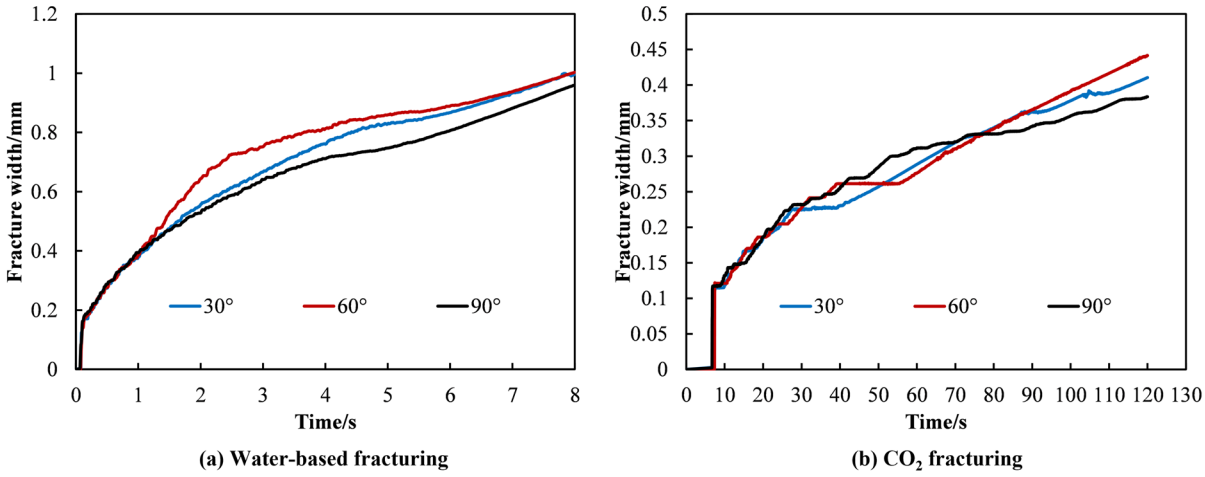


Figure 9. The fracture width evolution during water-based fracturing and $ScCO_2$ fracturing under different natural fracture approach angles.

4.4. The Effect of Injection Rate on the Fracture Network Development

To further investigate the effect of $ScCO_2$ on the formation of complex fracture networks, a two-dimensional model containing a pre-existing discrete natural fracture network was established. A total of 82 pre-existing natural fractures with a length of 2 m were generated using a uniform distribution function, with fracture orientations uniformly distributed between 0° and 180°. Figure 10 shows the fracture propagation patterns of $ScCO_2$ fracturing in the complex discrete natural fracture network under different injection rates. The results show that, in the complex natural fracture network, CO_2-driven fractures no longer exhibit a simple bi-wing symmetric propagation pattern, but are strongly controlled by the orientations and spatial distribution of the pre-existing natural fractures. During propagation, the main fracture intersects with natural fractures multiple times and undergoes deflection, step-like propagation, and local connection along locally favorable natural fracture directions, thereby forming a complex fracture path with pronounced tortuosity. All three cases exhibit strong natural fracture activation, but the fracture propagation direction and connectivity range differ among different injection rates. Under the low injection-rate condition, the fractures show obvious deflection on both sides of the injection point and are strongly controlled by the orientations of the natural fractures, resulting in a relatively complex fracture geometry. At an injection rate of 0.001 m^3/s, the hydraulic fracture still mainly propagates along the discrete natural fracture network in a continuous step-like pattern toward the upper-right direction. When the injection rate further increases to 0.002 m^3/s, although some natural fractures are still activated, the hydraulic fracture shows a stronger tendency to propagate along the direction of the maximum horizontal principal stress. In terms of fracture-width distribution, the fracture aperture is mainly concentrated in the main fracture and the local regions connected with natural fractures, whereas the branch fractures propagating along natural fractures exhibit relatively smaller apertures. This indicates that the low viscosity of CO_2 facilitates its invasion into natural fractures and induces weak-plane activation; however, fluid diversion and pressure dissipation within the complex fracture network limit the aperture growth of individual fractures.

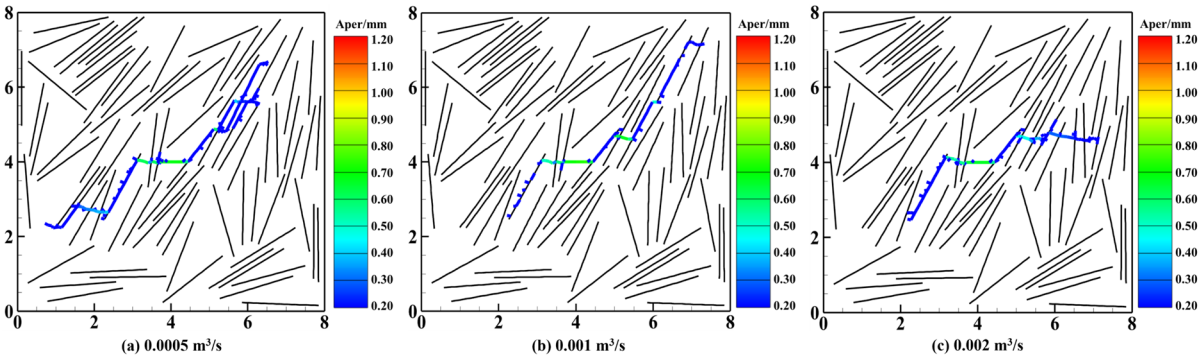


Figure 10. The fracture propagation patterns of $ScCO_2$ fracturing in the complex discrete natural fracture network under different injection rates.

Figure 11 quantitatively compares the variations in hydraulic fracture length, activated natural fracture length, and their corresponding fracture areas under different injection rates. As the injection rate increases from 0.0005 m^3/s to 0.001 m^3/s, the total fracture length decreases markedly from 15.6 m to 10.8 m. When the injection rate further increases to 0.002 m^3/s, the total fracture length remains nearly stable; however, the hydraulic fracture length increases, whereas the activated natural fracture length further decreases. This indicates that, under a lower injection rate, CO_2 has more sufficient time to invade natural fractures and weak planes, thereby promoting natural fracture opening or shear activation. In contrast, under a higher injection rate, more fluid energy is concentrated on the rapid propagation of the main hydraulic fracture, resulting in a relatively lower degree of natural fracture activation. In terms of fracture area, the hydraulic fracture area dominates the total fracture area, whereas the area of activated natural fractures is relatively small. The variation in total fracture area with injection rate is less pronounced than that in fracture length, indicating that the injection rate has a stronger influence on fracture extension range and activated natural fracture length than on overall fracture aperture or fracture area. Overall, a lower injection rate is more favorable for sufficient interaction between CO_2 and natural fractures, leading to the formation of a longer fracture network. A higher injection rate promotes main-fracture propagation but reduces the contribution of activated natural fractures to the overall fracture network.

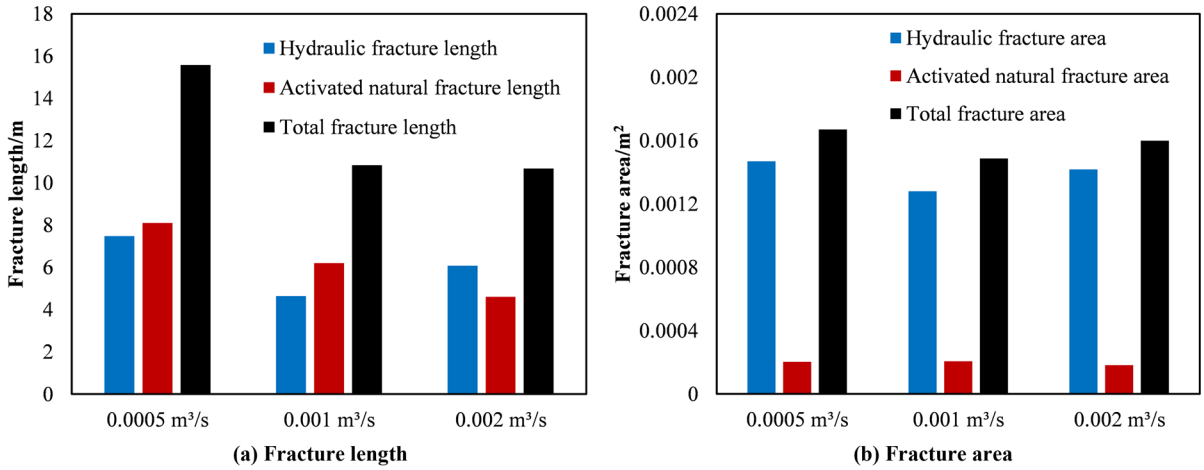


Figure 11. The hydraulic fracture length, activated natural fracture length, and the fracture areas under different injection rates.

4.5. The Effect of Stress Difference on the Fracture Network Development

Figure 12 shows the fracture propagation patterns of $ScCO_2$ fracturing in the complex discrete natural fracture network under different horizontal stress differences. The results show that the stress difference has a significant influence on the propagation direction of the main fracture, the extent of natural fracture activation, and the connectivity of the fracture network. Under a low stress difference, the *in-situ* stress anisotropy is relatively weak, and fracture propagation is more strongly controlled by the discrete natural fracture network. In this case, CO_2-driven fractures are more likely to deflect and extend along favorably oriented natural fractures, forming obliquely connected fracture pathways involving multiple natural fractures. The activated natural fracture region is relatively extensive, indicating that a low stress difference weakens the constraint imposed by the principal stress direction and promotes sufficient interaction between CO_2 and the natural fracture network. As the stress difference increases, the control of the maximum horizontal principal stress on fracture propagation gradually becomes stronger. The overall propagation direction becomes more stable, and the degree of large-scale deflection along natural fractures decreases. Under a moderate stress difference, the main fracture can still connect multiple natural fractures and form a relatively continuous step-like propagation path, indicating that fracture growth is jointly controlled by main-fracture propagation and natural fracture activation. Under a high stress difference, the fracture shows a stronger tendency to propagate along the principal stress direction. Natural fracture activation is mainly concentrated near the main fracture and local intersection regions, whereas the participation of natural fractures away from the main-fracture path becomes relatively limited. Nevertheless, owing to the low viscosity of CO_2 and its strong ability to invade weak planes, local natural fracture opening and branch propagation can still be induced under a high stress difference. Overall, the fracture network under high stress-difference conditions is characterized by enhanced stress guidance and localized natural fracture activation.

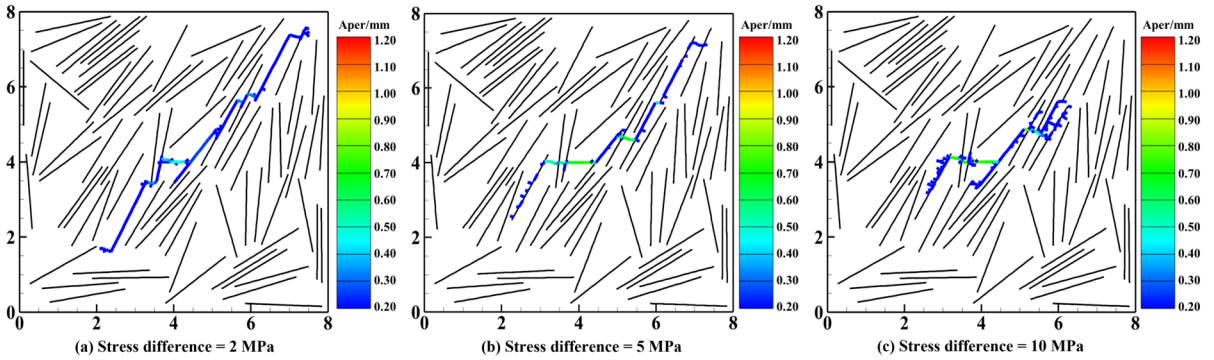


Figure 12. The fracture propagation patterns of $ScCO_2$ fracturing in the complex discrete natural fracture network under different horizontal stress differences.

Figure 13 further quantitatively compares the variations in hydraulic fracture length, activated natural fracture length, and their corresponding fracture areas under different stress differences. As the stress difference increases from 2 MPa to 10 MPa, the hydraulic fracture length gradually increases, whereas the activated natural fracture length generally decreases. Under the low stress-difference condition, the activated natural fracture length is significantly greater than the hydraulic fracture length, indicating that CO_2 more readily invades and activates natural fractures when the *in-situ* stress anisotropy is weak. In this case, fracture propagation is more strongly controlled by the discrete natural fracture network. As the stress difference increases, the guiding effect of the maximum horizontal principal stress on fracture propagation becomes stronger, which enhances the extension of the main hydraulic fracture while suppressing the activation of natural fractures away from the main-fracture path. In terms of fracture area, the activated natural fracture area is close to the hydraulic fracture area under the 2 MPa condition, suggesting that natural fractures make a substantial contribution to the overall fracture network. When the stress difference increases to 5 MPa and 10 MPa, the hydraulic fracture area increases significantly, whereas the activated natural fracture area decreases markedly. This indicates that the fracture network gradually shifts from being dominated by natural fracture activation to being dominated by main hydraulic fracture propagation. Although the total fracture area varies only slightly under different stress differences, the fracture composition changes considerably: a low stress difference favors the formation of a complex fracture network with a higher contribution from activated natural fractures, whereas a high stress difference promotes directional main-fracture extension and aperture growth. Overall, increasing the stress difference strengthens the control of the principal stress direction on CO_2-driven fracture propagation, leading to a transition in the propagation mode from natural fracture-controlled growth to main-fracture-controlled growth.

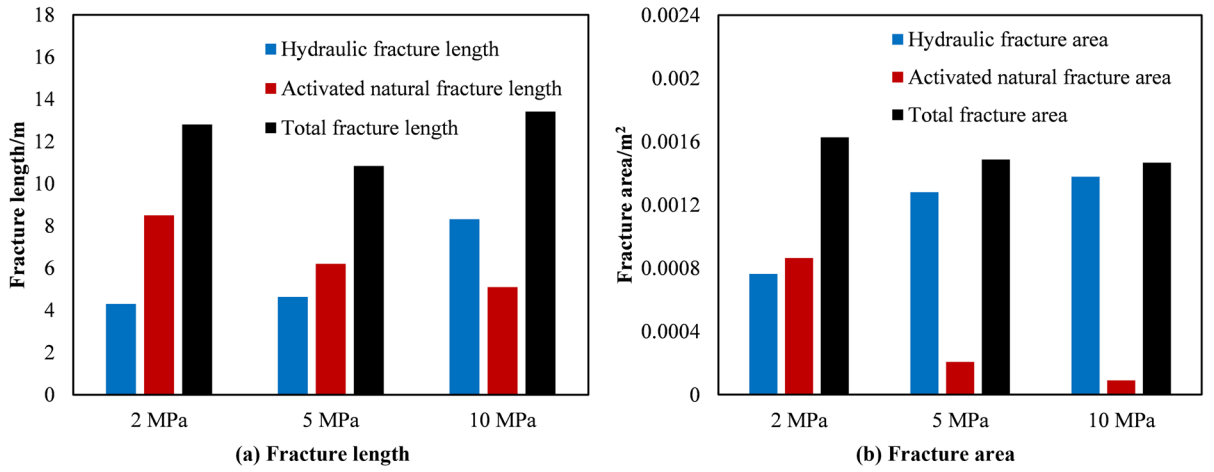


Figure 13. The hydraulic fracture length, activated natural fracture length, and the fracture areas under different horizontal stress differences.

5. Conclusions

(1) Under the same symmetric natural-fracture configuration, water-based fracturing and $ScCO_2$ fracturing exhibit distinct fracture-propagation behaviors. Water-based fracturing is characterized by rapid pressure buildup, a relatively straight main fracture, and larger fracture width. In contrast, $ScCO_2$ fracturing shows

delayed pressure response, stronger pressure fluctuations, more pronounced natural-fracture activation, and tortuous step-like fracture paths. The fracture width generated by $ScCO_2$ fracturing is smaller, which is mainly attributed to its low viscosity, stronger flow capacity, and enhanced fluid diversion into pre-existing natural fractures.

(2) Horizontal principal stress difference and natural-fracture approach angle jointly control the interaction between hydraulic fractures and natural fractures. A lower stress difference weakens the guidance of the maximum horizontal principal stress and promotes fracture deflection, natural-fracture opening, and complex fracture-network formation. As the stress difference increases, the main fracture tends to propagate more stably along the maximum horizontal principal stress direction. Low natural-fracture approach angles favor fracture capture and deflection along pre-existing weak planes, whereas high approach angles promote direct crossing and relatively simple fracture geometries.

(3) In complex discrete natural-fracture networks, $ScCO_2$-driven fracture propagation is strongly affected by injection rate, stress difference, and natural-fracture topology. A lower injection rate allows $ScCO_2$ to interact more sufficiently with natural fractures, thereby increasing the activated natural-fracture length and fracture-network tortuosity. A higher injection rate enhances the extension of the main hydraulic fracture but reduces the contribution of activated natural fractures. Increasing the horizontal stress difference further shifts the propagation mode from natural-fracture-controlled growth to main-fracture-controlled growth.

Author Contributions

G.H.: conceptualization, methodology, software, formal analysis, visualization, and writing—original draft preparation; F.Z.: conceptualization, supervision, funding acquisition, and writing—review and editing; B.Z.: supervision and writing—review and editing; M.L.: methodology and writing—review and editing; Y.H.: data curation; G.L.: investigation and writing—review and editing. All authors have read and agreed to the published version of the manuscript.

Funding

This research was funded by the National Natural Science Foundation of China [No. U23B2084] and the Innovative Research Group Project of National Natural Science Foundation of China [No. 52421002].

Data Availability Statement

Data will be made available on request.

Conflicts of Interest

The authors declare no conflict of interest.

Use of AI and AI-Assisted Technologies

During the preparation of this manuscript, the authors used ChatGPT (OpenAI) for grammar checking and language polishing. The authors reviewed and edited the content as necessary and take full responsibility for the content of the published article.

References

1. Gao, X.; Yang, S.; Zhang, Y.; et al. Integrated modeling and economic assessment of hydrogen storage with wellbore-reservoir-thermo-hydro-mechanical-diffusion coupling. *Energy* **2026**, *353*, 141065. https://doi.org/10.1016/j.energy.2026.141065.
2. Hou, L.; Zhang, S.; Elsworth, D.; et al. Review of fundamental studies of CO_2 fracturing: Fracture propagation, propping and permeating. *J. Pet. Sci. Eng.* **2021**, *205*, 108823. https://doi.org/10.1016/j.petrol.2021.108823.
3. Middleton, R.S.; Carey, J.W.; Currier, R.P.; et al. Shale gas and non-aqueous fracturing fluids: Opportunities and challenges for supercritical CO_2. *Appl. Energy* **2015**, *147*, 500–509. https://doi.org/10.1016/j.apenergy.2015.03.023.
4. Li, Y.; Peng, G.; Tang, J.; et al. Thermo-hydro-mechanical coupling simulation for fracture propagation in CO_2 fracturing based on phase-field model. *Energy* **2023**, *284*, 128629. https://doi.org/10.1016/j.energy.2023.128629.
5. Chen, H.; Kang, Y.; Jin, W.; et al. Numerical modeling of fracture propagation of supercritical CO_2 compound fracturing. *J. Rock Mech. Geotech. Eng.* **2024**, *16*, 2607–2628. https://doi.org/10.1016/j.jrmge.2023.11.043.
6. Sun, Y.X.; Wang, X.L.; Meng, Y.Z.; et al. Fracture propagation mechanism and application of supercritical CO_2 fracturing in shale: A review. *Pet. Sci.* **2025**, *22*, 1625–1652. https://doi.org/10.1016/j.petsci.2025.01.009.

7. Huang, G.; Li, M.; Chu, J.; et al. Longitudinal propagation mechanisms of multiple fractures in heterogeneous multi-lithology stacked reservoirs: A continuum-discontinuum simulation study. *Eng. Fract. Mech.* **2025**, *322*, 111181. https://doi.org/10.1016/j.engfracmech.2025.111181.
8. Huang, G.; Zhou, F.; Zhang, B.; et al. Visual experimental investigation on dynamic propagation mechanisms of multi-fractures in layered media. *Int. J. Rock Mech. Min. Sci.* **2026**, *205*, 106601. https://doi.org/10.1016/j.ijrmms.2026.106601.
9. Huang, G.; Li, M.; Zhou, F.; et al. Numerical simulation of multi-fracture uniform propagation in naturally fractured reservoirs based on the continuum–discontinuum method. *Phys. Fluids* **2024**, *36*, 037111. https://doi.org/10.1063/5.0194485.
10. Zhang, Z.; Yu, H.; Li, B.; et al. A multi-processes phase-field model for CO_2 phase change fracturing. *Int. J. Rock Mech. Min. Sci.* **2026**, *198*, 106363. https://doi.org/10.1016/j.ijrmms.2025.106363.
11. Zhao, H.; Wu, K.; Huang, Z.; et al. Numerical model of CO_2 fracturing in naturally fractured reservoirs. *Eng. Fract. Mech.* **2021**, *244*, 107548. https://doi.org/10.1016/j.engfracmech.2021.107548.
12. Zhao, Z.; Li, X.; He, J.; et al. A laboratory investigation of fracture propagation induced by supercritical carbon dioxide fracturing in continental shale with interbeds. *J. Pet. Sci. Eng.* **2018**, *166*, 739–746. https://doi.org/10.1016/j.petrol.2018.03.066.
13. Dahi Taleghani, A.; Gonzalez, M.; Shojaei, A. Overview of numerical models for interactions between hydraulic fractures and natural fractures: Challenges and limitations. *Comput. Geotech.* **2016**, *71*, 361–368. https://doi.org/10.1016/j.compgeo.2015.09.009.
14. Hu, Y.; Gan, Q.; Hurst, A.; et al. Investigation of coupled hydro-mechanical modelling of hydraulic fracture propagation and interaction with natural fractures. *Int. J. Rock Mech. Min. Sci.* **2023**, *169*, 105418. https://doi.org/10.1016/j.ijrmms.2023.105418.
15. Zhou, J.; Zhang, L.; Braun, A.; et al. Investigation of Processes of Interaction between Hydraulic and Natural Fractures by PFC Modeling Comparing against Laboratory Experiments and Analytical Models. *Energies* **2017**, *10*, 1001. https://doi.org/10.3390/en10071001.
16. Zang, Y.X.; Li, F.X.; Wang, H.Z.; et al. Effect of CO_2 pre-injection on fracture propagation morphology in shale reservoirs under CO_2 hybrid fracturing. *Pet. Sci.* **2026**, *23*, 2698–2712. https://doi.org/10.1016/j.petsci.2026.01.031.
17. Jiang, C.; Chen, J.; Wang, H.; et al. Phase-field simulation of CO_2 fracturing crack propagation in thermo-poroelastic media. *Int. J. Rock Mech. Min. Sci.* **2025**, *187*, 106052. https://doi.org/10.1016/j.ijrmms.2025.106052.
18. Li, Y.; Hu, W.; Zhang, Z.; et al. Numerical simulation of hydraulic fracturing process in a naturally fractured reservoir based on a discrete fracture network model. *J. Struct. Geol.* **2021**, *147*, 104331. https://doi.org/10.1016/j.jsg.2021.104331.
19. Huang, G.; Hu, X.; Zhou, F.; et al. A New Multi-Cluster Fracturing Simulation Model Coupled with Perforation Erosion: Based on the Continuous–Discontinuous Method. *Rock Mech. Rock Eng.* **2023**, *56*, 3887–3901. https://doi.org/10.1007/s00603-023-03256-9.
20. Zhang, B.; Guo, T.; Chen, M.; et al. Research on fracture propagation of hydraulic fracturing in a fractured shale reservoir using a novel CDEM-based coupled HM model. *Comput. Geotech.* **2024**, *168*, 106170. https://doi.org/10.1016/j.compgeo.2024.106170.
21. Zhu, X.; Feng, C.; Cheng, P.; et al. A novel three-dimensional hydraulic fracturing model based on continuum–discontinuum element method. *Comput. Methods Appl. Mech. Eng.* **2021**, *383*, 113887. https://doi.org/10.1016/j.cma.2021.113887.
22. Ren, Q.; Zhao, Y.; Zhu, X.; et al. CDEM-based simulation of the 3D propagation of hydraulic fractures in heterogeneous Coalbed Methane reservoirs. *Comput. Geotech.* **2022**, *152*, 104992. https://doi.org/10.1016/j.compgeo.2022.104992.